

# Simultaneous Multiple Object Detection and Pose Estimation using 3D Model Infusion with Monocular Vision

Congliang Li \*  
Chang'an University  
Xi'an, Shannxi, China  
congliangli@chd.edu.com

Shijie Sun \*  
Chang'an University  
Xi'an, Shannxi, China  
shijieSun@chd.edu.cn

Xiangyu Song †  
Swinburne University of Technology  
Melbourne, Australia  
xsong@swin.edu.au

Huansheng Song  
Chang'an University  
Xi'an, Shannxi, China  
hshsong@chd.edu.cn

Naveed Akhtar  
University of Western Australia  
Perth, Western Australia, Australia  
naveed.akhtar@uwa.edu.au

Ajmal Saeed Mian  
University of Western Australia  
Perth, Western Australia, Australia  
ajmal.mian@uwa.edu.au

## Abstract

*Multiple object detection and pose estimation are vital computer vision tasks. The latter relates to the former as a downstream problem in applications such as robotics and autonomous driving. However, due to the high complexity of both tasks, existing methods generally treat them independently, which is sub-optimal. We propose simultaneous neural modeling of both using monocular vision and 3D model infusion. Our Simultaneous Multiple Object detection and Pose Estimation network (SMOPE-Net) is an end-to-end trainable multitasking network with a composite loss that also provides the advantages of anchor-free detections for efficient downstream pose estimation. To enable the annotation of training data for our learning objective, we develop a Twin-Space object labeling method and demonstrate its correctness analytically and empirically. Using the labeling method, we provide the KITTI-6DoF dataset with  $\sim 7.5K$  annotated frames. Extensive experiments on KITTI-6DoF and the popular LineMod datasets show a consistent performance gain with SMOPE-Net over existing pose estimation methods. Here are links to our proposed SMOPE-Net, KITTI-6DoF dataset, and LabelImg3D labeling tool.*

\*The first two authors contributed equally to this paper.

†Corresponding authors.

## 1. Introduction

Multiple Object Detection (MOD) and Pose Estimation (PE) are critical machine perception tasks for intelligent systems. Recent literature has witnessed multiple interesting contributions for MOD [35, 37, 43]. However, the state-of-the-art of MOD is still considered insufficient for many application domains, e.g., robotics [2, 11], autonomous driving [6, 22, 23], virtual reality [1, 9] and database engineering [10]. In these domains, PE - a.k.a. 6 Degree of Freedom (6DoF) estimation - is normally performed as a downstream task of MOD. Partially owing to the inadequacy of MOD performance, the vast majority of existing related literature employs methods that treat the two tasks independently [26, 27, 33].

Considering the strong relationship between the object poses and the ability to detect them, we conjecture that the downstream PE task should strongly benefit from the upstream detection task. Evidence is already available that unifying the two tasks can help in better pose estimation [5]. However, the method of [5] must use anchor boxes for object detection. Inaccurate selection of anchor boxes can lead to even worse pose estimation than the methods that treat the two problems independently [26, 27, 33].

In this work, we introduce Simultaneous Multiple Object detection and Pose Estimation (SMOPE) that is implemented as a single-stage multi-tasking neural network (SMOPE-Net) allowing anchor-free object detection - Fig. 1. SMOPE-Net solves a highly complex problem,

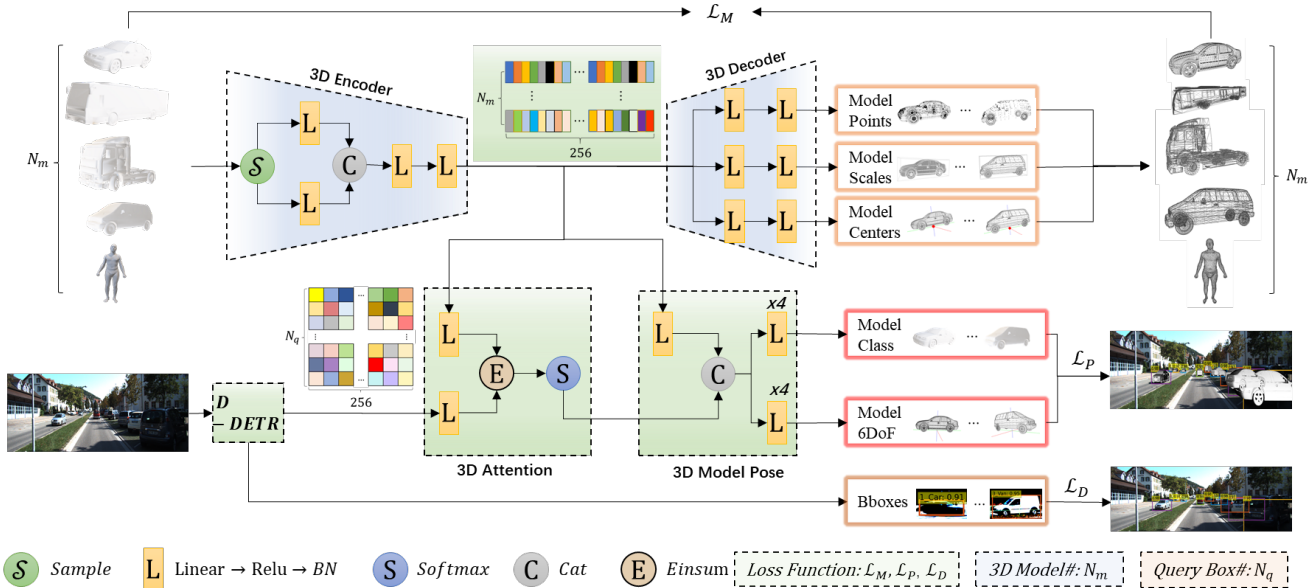


Figure 1. SMOPE-Net schematics: The network takes images and  $N_m$  3D object models as input. The Deformable-DETR (D-DETR) provides a 256-dim feature vector for each of the  $N_q$  queries and the detected bounding boxes (Bboxes) for the input under the loss  $\mathcal{L}_D$ . A 3D Encoder learns a 256-dim latent space. The features of  $N_m$  models in this space are used by the 3D Decoder to estimate model points, scales, and centers to reconstruct the  $N_m$  models under the loss  $\mathcal{L}_M$ . The  $N_m \times 256$  features are also used by the 3D Attention module to compute attention maps for the queries, and the 3D Model Pose module to predict model class and object 6DoF pose estimates. Both components are used for computing the  $\mathcal{L}_P$  loss. Inference is performed on a single RGB image using only part of the network within the green background. The learned  $N_m \times 256$  embeddings are used and the 3D models/Encoder/Decoder are no longer required.

for which the existing datasets for MOD and PE [16, 39] are insufficient, especially for the key application domain of traffic scenes. To address that, we develop a **Twin-space Object Pose Labeling (TOPL)** method for efficient, yet accurate 6DoF annotation of images. This method is realized as a tool, LabelImg3D, which also addresses the gap of lack of public annotation tool for the problem. Applying LabelImg3D on KITTI dataset [13], we publish a traffic MOD&PE dataset (KITTI-6DoF) which provides additional annotations (details in Sec. 3.4). The dataset can be used for MOD and PE tasks independently, or for learning joint models like SMOPE-Net.

The contributions of this paper can be summarized as:

- We realize Simultaneous Multiple Object detection and Pose Estimation (SMOPE) with an anchor-free multi-tasking neural network SMOPE-Net.
- We propose a Twin-space Object Labeling (TOPL) method for 6DoF labeling of objects in 2D images. The method is packaged as a tool - LabelImg3D.
- We introduce KITTI-6DoF dataset for the 6DoF pose estimation task. The dataset provides an order of magnitude increased distance between the object and camera as compared to the existing datasets [16], [39], which is highly desirable for the key application domain of traffic scene analysis.
- We demonstrate that SMOPE-Net outperforms existing methods on the challenging LineMod [4], and

KITTI-6DoF datasets, using only a single image, requiring no masks. This offers new possibilities for practical MOD&PE.

## 2. Related Work

We review related literature along 6DoF estimation task, 2D object detection problem, and the related datasets. These topics form the core of our contributions.

### 2.1. 6Dof Estimation

**Direct estimation of 6DoF pose:** The most direct strategy to estimate 6DoF pose of a target object is to regress it with a network, e.g. PoseCNN [39] and EfficientPose [5]. These methods regress the rotation and displacement parameters using neural models and deal with symmetric objects to solve the rotation error problem that occurs when the target is symmetric. The SSD6D method [20] discretizes the continuous rotation space into bins and classifies them by extending the 2D target detection method SSD [24]. Similarly, [34] learns the implicit rotation representation with an autoencoder. However, due to discretization, a high-level of refinement is necessary to obtain a relatively accurate 6DoF pose.

**2D detection and Perspective-n-Point (PnP) methods:** Currently, the methods showing higher accuracy for the 6DoF task mainly employ 2D object detection and PnP estimation. Such methods can be broadly categorized into

two types: key point based detection methods [26, 27, 33] and dense 2D-3D correspondence methods [40]. The former generally selects the vertices of the target 3D envelope frame or the points on the surface of a 3D model as the key points. The key points of an envelope frame are not on the object’s surface, hence, they do not require a 3D model. However, their prediction is challenging, even with well-known techniques [5]. Since some key points may not be on the object due to, e.g. occlusion, researchers have also proposed a pixel-by-pixel voting scheme to predict the vector of each pixel pointing to the key point [26]. They finally use RANSAC to find the key point location. The dense 2D-3D correspondence method [40] predicts 3D model points corresponding to each 2D pixel of an object. These correspondences are generally obtained with a UV mapping or regression of the object’s coordinates in 3D model space. The 6D pose is then computed with PnP or RANSAC.

## 2.2. Object Detection

The literature in 2D object detection with neural models is currently divided into two-stage [32] and one-stage [25] techniques. The two-stage methods, such as R-CNN [15], Fast-R-CNN [14], Faster-R-CNN [29], etc., usually achieve higher accuracy. However, one-stage approaches, such as SSD [24], YOLO [44], RefineDet [41], etc., are known for their higher detection speed. Most one-stage methods lack leveraging global frame features, which compromises their performance. More recently, Carion et al. [7] used Transformers in their DETR detection network to account for the global image features in its encoder-decoder architecture. This improved detection performance while maintaining the model scalability. Inspired, we also take advantage of the DETR detection in our model for the proposed SMOPE.

## 2.3. Related Datasets

The vast majority of existing datasets for object pose estimation first obtain the object depth by an RGB-D camera [8] and then derive the object 6DoF pose. The current publicly available datasets, LineMod (LM) [16], Line Mod-Occluded (LM-O) [4], Rutgers APC (RU-APC) [30], T-LESS [17], YCB- Video (YCB-V) [39], HomebrewedD B (HB) [19], all follow this strategy.

The 6DoF dataset LineMod [16] is free of occlusions and adopts a random positional approach for the acquisition of scene. [4] released the LineMod-O dataset that introduced occlusion scenes in LineMod. [30] proposed RU-APC to broaden the application scenario of positional estimation methods by introducing an occlusion scenario related to the shelves of a warehouse. [17] presented T-LESS, where models have prominent symmetry and no obvious texture, making pose estimation more challenging. [39] proposed the YCB-V dataset, which converts the model coordinate units from meters to millimeters, and introduces the concept of 3D bounding box center and model coordinate system, so

that it can reflect the pose of real objects. HB [19] is another related dataset example for the pose estimation problem.

In the existing datasets, small camera-to-object distance is a frequently encountered shortcoming, which is rooted in the RGB-D sensor’s limited range. Therefore, we develop the TOPL method that only requires RGB images which have a much longer range, and employs 3D models of real objects to achieve the acquisition of the target 6D pose. This enables us to curate a dataset that has orders of magnitude larger camera-to-object distances compared to the datasets captured with 3D sensors.

## 3. Proposed Method

For the MOD&PE task, we propose a single-stage anchor-free SMOPE-Net which leverages image and 3D model deep features. Moreover, we devise a Twin-space Object Pose Labeling (TOPL) method and implement it as LabelImg3d tool that enables efficient object pose annotation in images.

### 3.1. SMOPE-Net

Figure 1 illustrates the overall architecture of the proposed network. The input consists of 3D object models and images. The 3D object models are required only for training. During inference, MOD&PE is performed using a single RGB image. Our goal is to detect the objects in the images and estimate the 6DoF of each detected object, which consists of rotation and translation matrices. The proposed network can be divided into five sub-networks; namely 3D Encoder, 3D Decoder, Deformable-DETR, 3D Attention, and 3D Model Pose estimation. Components required for inference are enclosed by green background in Fig. 1. Details of the sub-networks are provided below.

#### 3.1.1 3D Encoder and Decoder Sub-networks

To extract features from the 3D models, we use 3D Encoder/Decoder sub-networks which are required only during the training stage. The input to Encoder is  $N_m$  real-sized 3D models. The latent space of the Encoder/Decoder network is used to provide features of the models to the 3D Attention and 3D Model Pose sub-networks. The Decoder also leverages the latent space to decode the  $N_m$  models by learning to output the model points, model scales, and their centers. As the first part of the Encoder/Decoder network, the Encoder uniformly samples the points and surface normals of the meshes to make all the models consistent. The sampled models are then processed by two Linear layers, one each for extracting features of the points and the normals. The extracted features are concatenated and subsequently processed by two linear layers to output the features in the latent space. The size of these features is  $N_m \times 256$ . The 3D Decoder receives these features and decodes them using three parallel branches. Each branch contains two Linear layers. These three branches output

the points, scales, and centers of the models, respectively. Combined, this reconstructs the decoded 3D models.

### 3.1.2 Deformable-DETR and 3D Attention

The Deformable-DETR improves the original DETR [7] by introducing reference points to reduce the number of parameters and enable faster convergence. In the proposed SMOPE-Net, we employ the Deformable-DETR to process images and output bounding boxes (BBoxes) and query boxes' features with dimension  $N_q \times 256$ , where  $N_q$  is the number of query boxes. We employ the 3D Attention sub-network to estimate the attention between the  $N_m$  3D models and the  $N_q$  query boxes by using their extracted features. The features of the query boxes and the models are processed by two Linear layers of the 3D Attention sub-networks in parallel. The dimensions of these feature matrices are  $N_q \times 256$  and  $N_m \times 256$ , respectively. We use the Einstein summation convention to sum the product of the outputs of the Linear layers along the feature dimensions. This is followed by a *softmax* operation. Finally, the 3D Attention sub-network outputs a  $N_q \times N_m$  attention map between the query boxes and the 3D models.

### 3.1.3 3D Model Pose

The 3D Model Pose sub-network fuses the attention map it receives from the 3D Attention sub-network with the features of the 3D models. It outputs the model category and the 6DoF matrix for each query box with the help of a stream of parallel Linear layers. The features of the models are first processed by one Linear layer, which are then concatenated with the attention map as the features of the query boxes. Afterwards, these features are processed by two streams of Linear layers, where each stream uses four Linear layers to compute the output.

## 3.2. SMOPE Loss

Since the SMOPE-Net is a multi-tasking network, its loss function can be divided into three parts according to the different tasks. We express the overall loss as

$$\mathcal{L} = \mathcal{L}_D + \mathcal{L}_M + \mathcal{L}_P, \quad (1)$$

where  $\mathcal{L}_D$ ,  $\mathcal{L}_M$  and  $\mathcal{L}_P$  are respectively the Multiple Object Detection (MOD) loss, 3D Model loss and the Pose Estimation loss. We use the original MOD loss of the Deformable-DETR. For conciseness, we refer the readers to [45] for the details of  $\mathcal{L}_M$  and provide discussion on the remaining two losses below.

### 3.2.1 The 3D Model Loss

Sub-loss  $\mathcal{L}_M$  is used to minimise the difference between the ground-truth model and the predicted model. As shown in Eq. 2,  $\mathcal{L}_M$  comprises different components that achieve this objective. We design  $\mathcal{L}_{psc}$ , which is an  $L_1$  loss over the

point scales and centers. Besides, to robustly constrain the models' points and normals, we further use four sub-losses; namely, the chamfer distance loss ( $\mathcal{L}_{cd}$ ), the mesh edge loss ( $\mathcal{L}_{me}$ ), the mesh normal consistency loss ( $\mathcal{L}_{mnc}$ ), and the mesh Laplacian smoothing loss ( $\mathcal{L}_{mls}$ ). This results in the following

$$\mathcal{L}_M = \alpha_1 \mathcal{L}_{psc} + \alpha_2 \mathcal{L}_{cd} + \alpha_3 \mathcal{L}_{me} + \alpha_4 \mathcal{L}_{mnc} + \alpha_5 \mathcal{L}_{mls}, \quad (2)$$

where  $\{\alpha_i | i = 1, \dots, 5\}$  are the weights.

The chamfer distance loss is a common metric that quantifies agreements between the point clouds of the ground truth model  $G$  and the predicted model  $P$ . Formally,

$$\mathcal{L}_{cd} = |G|^{-1} \sum_{(g,p) \in \Lambda_{G,P}} \|g - p\|^2 + |P|^{-1} \sum_{(p,g) \in \Lambda_{P,G}} \|p - g\|^2, \quad (3)$$

where  $\Lambda_{G,P} = \{(g, \operatorname{argmin}_p \|g - p\|) | g \in G, p \in P\}$  is the set of pairs  $(g, p)$  such that  $g$  is the nearest neighbor of  $p$ .

The mesh edge loss computes mesh edge length regularization loss averaged across all the meshes. Formally,

$$\mathcal{L}_{me} = \frac{1}{\|E_p\|_0} \sum_{(p_0, p_1) \in E_p} \|p_0 - p_1\|_2^2, \quad (4)$$

where  $E_p$  is the set of edges in the predicted models and  $p_0, p_1$  are the start and end points of the edge.

The mesh normal consistency loss ensures that the normals in the predicted models are consistent for each mesh. It is formally given as

$$\mathcal{L}_{mnc} = \frac{1}{\|N_p\|_0} \sum_{(n_i, n_j) \in N_p} [1 - \cos(n_i, n_j)], \quad (5)$$

where  $N_p$  denotes the pair normals of  $F_p$  s.t.  $F_p = \{(f_i, f_j) | f_i \cap f_j \in E_p\}$ , and  $n_i, n_j$  are the normals.

Finally, the mesh Laplacian smoothing loss ( $\mathcal{L}_{mls}$ ) enables Laplacian smoothing of the predicted meshes. It is expressed as

$$\mathcal{L}_{mls} = \sum_{v_i \in V} \left\| \sum_{v_j \in N_i} \frac{1}{\|N_i\|_0} (v_j - v_i) \right\|_2, \quad (6)$$

where  $V$  is the points set of the mesh,  $v_i$  is the  $i$ -th point of  $V$ , and  $N_i$  is the neighboring points set of  $v_i$ .

### 3.2.2 Pose Estimation Loss

The 3D Model Pose sub-network predicts the category and 6DoF estimate of the query boxes. Its loss is also a compound loss, given in Eq. (7). It consists of two components; namely, the classification loss ( $\mathcal{L}_{cl}$ ) and the 6DoF loss ( $\mathcal{L}_{6d}$ ). With weights  $\gamma_1, \gamma_2$ , the loss is defined as

$$\mathcal{L}_P = \gamma_1 \mathcal{L}_{cl} + \gamma_2 \mathcal{L}_{6d}, \quad (7)$$

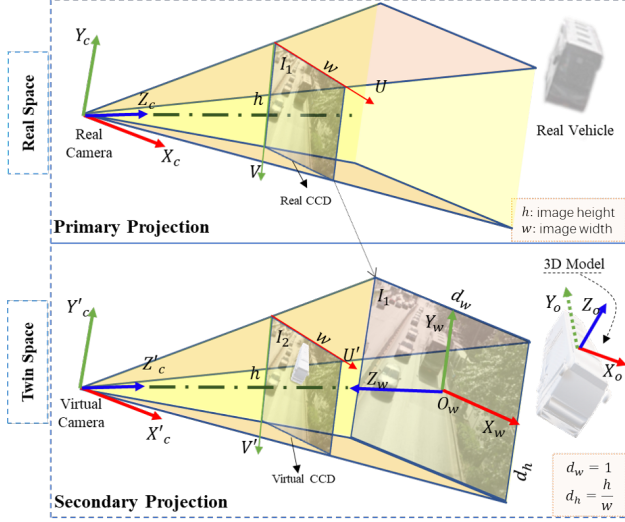


Figure 2. TOPL method: In Primary Projection, a real camera captures real objects in the real world. A virtual Twin Space is built to simulate that. This space contains 3D models, a virtual camera with the same focal length as the real camera and the captured image. In Secondary Projection, the virtual camera captures the 3D models and the image in the Twin Space.  $X_c Y_c Z_c, U V$  are the camera and image coordinates for the real scene.  $X'_c Y'_c Z'_c, U' V'$ ,  $X_w Y_w Z_w, X_o Y_o Z_o$  are the camera, image, world, and the model object coordinates in the Twin Space, respectively.

where  $\mathcal{L}_{cd}$  is the standard Cross-Entropy loss [42]. The 6DoF loss minimizes the difference between the translation and rotation of the predicted models and their ground truth counterparts. This loss is expressed as

$$\mathcal{L}_{6d} = \mathcal{L}_{fps} + \|p_p - p_g\|_1 + \|v_p - v_g\|_1, \quad (8)$$

where  $\mathcal{L}_{fps}$  is the farthest point sampling loss [35],  $p_p, p_g$  are the center points of the predicted and the ground truth models, and  $v_p, v_g$  are the quaternions of the predicted and the ground truth models, respectively.

### 3.3. Twin-space Object Pose Labeling (TOPL)

Considering the complexity of the underlying learning objective of SMOPE-Net, it is imperative to have appropriately annotated data for training the model. We propose a Twin-space monocular vision Object Pose Labeling (TOPL) method to facilitate such datasets. TOPL can compute translation and rotation annotations of objects in an image by directly using 3D models of the objects. The main concept of the method is illustrate in Fig. 2. We provide more details below, and formally prove the correctness of the method in the supplementary material.

#### 3.3.1 Method Details

TOPL uses the concept of Primary and Secondary Projections. In our context, the Primary Projection is the process

Table 1. Comparison of our KITTI-6DoF dataset to the original KITTI 3D object detection dataset. The latter does not provide Pitch and Roll angles, and nor does it provide 3D models.

|           | Position | Yaw | Pitch | Roll | 3D Model | 3D Size |
|-----------|----------|-----|-------|------|----------|---------|
| KITTI [3] | ✓        | ✓   | ×     | ×    | ×        | ✓       |
| Ours      | ✓        | ✓   | ✓     | ✓    | ✓        | ✓       |

of a camera capturing the objects in a real scene. Analogously, the Secondary Projection is the process of a virtual camera capturing the 3D model and image in our virtual Twin Space.

It is hard to directly estimate the pose of an object using only the Primary Projection. Hence, we use the virtual Twin Space where three entities are used. (i) A virtual camera (with focal length equal to that of the real camera) placed in a specified position. (ii) The captured image placed in the  $X_w O_w Y_w$  plane. (iii) 3D models with the same size as the real-world objects, see Fig. 2 (Twin Space). This configuration allows us to estimate the pose of the object via the Secondary Projection. Step-by-step process of this computation is discussed below.

**Step 1:** Twin Space is first generated using the VTK library utility for 3D software design [31]. The virtual camera is placed at the world coordinates  $(0, 0, d)$ , with a focal length ‘ $f$ ’ (equal to that of the real camera). The camera’s optical axis is oriented opposite to  $z$ -axis of the world coordinates, see  $Z_w$  in the Figure.

**Step 2:** The image generated by the Primary Projection is placed at the position where it exactly fills the range of the virtual camera. As illustrated in Fig. 2, to compare the Real Space image  $I_1$  with the Twin Space image  $I_2$ , we place  $I_1$  in the Twin Space such that it satisfies the following conditions: (i)  $I_1$  is scaled to  $1 \times \frac{h}{w}$ . (ii)  $I_1$  is in the  $X_w O_w Y_w$  plane. (iii) The center point of  $I_1$  is placed at  $O_w$ . (iv) The  $U$  axis of  $I_1$  is parallel to the  $X_w$  axis, and (v) the  $V$  axis of  $I_1$  is parallel to the  $Y_w$  axis.

**Step 3:** The object models are placed in the field of view (FoV) of the virtual camera making them available to be captured by the Secondary Projection of the virtual camera.

**Step 4:** By transforming the 3D models in the FoV of the camera, the 3D models in  $I_2$  are corresponded to the objects in  $I_1$ . This way, the poses of the 3D models are the same as the poses of their corresponding objects in the image. The poses of the 3D models are then acquired by the VTK tool.

The TOPL method allows us to estimate the correct poses - see supplementary material - of real objects with help of 3D models in a virtual twin space. The method is implemented and packaged as an annotation tool, ‘‘LabelImg3D’’, which will be made public.

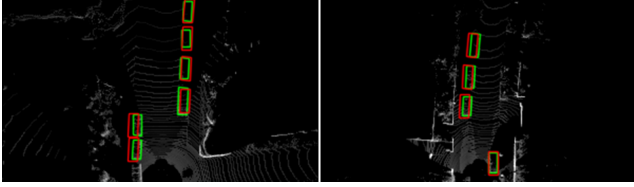


Figure 3. Consistency of KITTI-6DoF annotations performed on 2D images (red boxes) compared to annotations performed on the LiDAR data (green boxes). We show the top view since the latter does not have pitch roll annotations (see Table 1).

Table 2. Comparison of 6DoF datasets. **O.N.**, **O.D.**, **C.O.D.** stand for the number of objects, the maximum diameter of objects, and the maximum distance from the camera to objects.

|            | Frames         | O.N.           | O.D. (m)      | C.O.D.(m)      |
|------------|----------------|----------------|---------------|----------------|
| L-M [16]   | 15,800         | 15,800         | 0.283         | 1.169          |
| YCB-V [39] | <b>133,827</b> | <b>613,917</b> | 0.325         | 1.582          |
| Ours       | 7,481          | 27,665         | <b>16.605</b> | <b>150.818</b> |

### 3.4. Proposed KITTI-6DoF dataset

With LabelImg3D, we label a subset of KITTI dataset [13] to create ‘‘KITTI-6DoF’’, providing additional annotations for the 6DoF estimation task for 5 object categories on 7,481 frames. In Table 1, we compare our KITTI-6DoF to the original KITTI 3D object detection dataset [3].

To accommodate realistic variation in the size of different vehicle classes, we assign the average size of the KITTI-labeled vehicle classes to the corresponding 3D models we use for training our network. In Fig. 3, we visually compare our KITTI-6DoF annotations performed on 2D images to those performed on 3D LIDAR data. We can notice the consistency between the labels. We also compare KITTI-6DoF with the existing datasets L-M [16] and YCB-V [39] in Table 2 to show its advantages in terms of object size and camera-to-object distance.

## 4. EXPERIMENTS

### 4.1. LabelImg3D Evaluation

We first evaluate the performance of LabelImg3D tool. Poses of objects can be fully represented by their coordinate values  $(x, y, z)$  and rotation angles  $(r_x, r_y, r_z)$ . A comprehensive evaluation of pose estimation is possible by the metrics measuring the differences of each of these components with their respective ground truths. We define these metrics as  $\iota_X = e^{-|x_l - x_g|}$ ,  $\iota_Y = e^{-|y_l - y_g|}$ ,  $\iota_Z = e^{-|z_l - z_g|}$  and  $\alpha_{RX} = \cos(r_{xg} - r_{xl})$ ,  $\alpha_{RY} = \cos(r_{yg} - r_{yl})$ ,  $\alpha_{RZ} = \cos(r_{zg} - r_{zl})$ . Here, the subscripts ‘g’ and ‘l’ respectively denote the ground-truth and the predicted labels. Using these metrics LabelImg3D is evaluated on LineMod [4] and KITTI [13] datasets.



Figure 4. Representative LineMod labeling results with LabelImg3D. Each image shows the labeling result for a different 3D model of an object. Best viewed enlarged.

Table 3. LabelImg3D performance on LineMod dataset

| Class | $\iota_X$ | $\iota_Y$ | $\iota_Z$ | $\alpha_{RX}$ | $\alpha_{RY}$ | $\alpha_{RZ}$ |
|-------|-----------|-----------|-----------|---------------|---------------|---------------|
| Ape   | 0.986     | 0.994     | 0.965     | 0.911         | 0.993         | 0.960         |
| Bench | 0.989     | 0.995     | 0.957     | 0.877         | 0.993         | 0.994         |
| Cat   | 0.985     | 0.994     | 0.949     | 0.981         | 0.932         | 0.899         |
| Duck  | 0.988     | 0.992     | 0.936     | 0.905         | 0.995         | 0.955         |
| Lamp  | 0.995     | 0.990     | 0.960     | 0.848         | 0.981         | 0.853         |
| Mean  | 0.988     | 0.993     | 0.953     | 0.904         | 0.979         | 0.922         |

Table 4. LabelImg3D performance on KITTI dataset

| Class      | $\iota_X$ | $\iota_Y$ | $\iota_Z$ | $\alpha_{RX}$ | $\alpha_{RY}$ | $\alpha_{RZ}$ |
|------------|-----------|-----------|-----------|---------------|---------------|---------------|
| Tram       | 0.605     | 0.877     | 0.826     | 0.998         | 0.868         | 0.998         |
| Car        | 0.955     | 0.939     | 0.944     | 0.999         | 0.997         | 0.999         |
| Van        | 0.913     | 0.905     | 0.938     | 0.994         | 0.988         | 0.993         |
| Truck      | 0.947     | 0.952     | 0.944     | 0.963         | 0.973         | 0.981         |
| Pedestrian | 0.895     | 0.937     | 0.972     | 0.909         | 0.938         | 0.866         |
| Mean       | 0.863     | 0.922     | 0.925     | 0.973         | 0.953         | 0.967         |

#### 4.1.1 LabelImg3D on LineMod

From the dataset, we randomly selected 200 samples and labeled them using LabelImg3D for each object category. Fig. 4 shows representative partially labeled images as examples. Quantitative results of LabelImg3D are summarized in Table 3. It is noticeable that each metric achieves reasonably high value. The translation parameters  $(\iota_X, \iota_Y, \iota_Z)$  in general have values very close to the ground truth (i.e.  $\rightarrow 1$ ). Similarly, the rotation parameters  $(\alpha_{RX}, \alpha_{RY}, \alpha_{RZ})$  also show values in acceptable ranges despite the highly challenging rotation estimate requirements of the complex objects in the dataset.

#### 4.1.2 LabelImg3D on KITTI

We divided the objects into 5 categories and labeled all of the images in KITTI 3D detection dataset. Visual examples of labeled images are in the supplementary material. Table 4 summarizes the quantitative results.

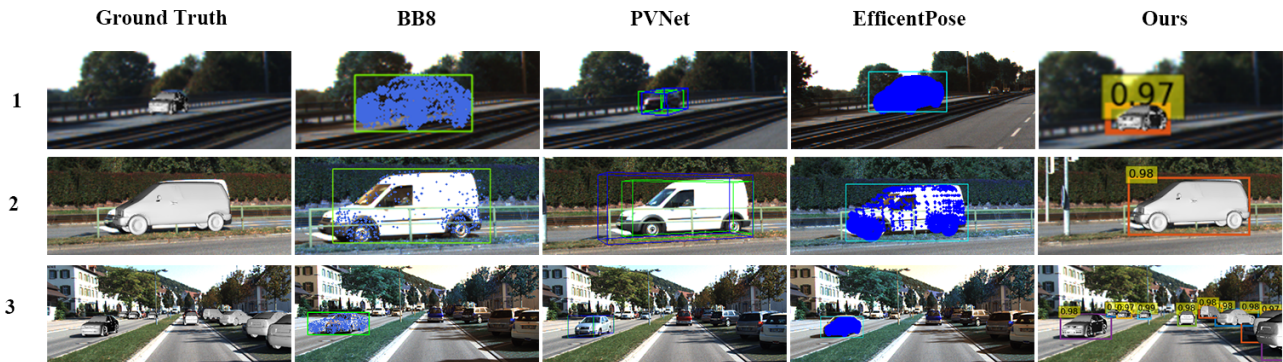


Figure 5. Qualitative results on KITTI-6DoF dataset. First column is ground truth generated by LabelImg3D. Notice that our method is more accurate and can detect all the cars in the 3rd row whereas all other methods detect only one. Best viewed in zoom in.

Table 5. Benchmarking on KITTI-6DoF dataset.  $\uparrow$  indicates larger value is more desirable,  $\downarrow$  shows lower value is better.

| CLASS  | BB8<br>[28]      |                        |                        |                        | PVNet<br>[26]    | EfficientPose<br>[5] |                        |                        |                        | Ours<br>(SMOPE-Net) |                        |                        |                        |
|--------|------------------|------------------------|------------------------|------------------------|------------------|----------------------|------------------------|------------------------|------------------------|---------------------|------------------------|------------------------|------------------------|
|        | $\iota \uparrow$ | $\eta_{RX} \downarrow$ | $\eta_{RY} \downarrow$ | $\eta_{RZ} \downarrow$ | $\iota \uparrow$ | $\iota \uparrow$     | $\eta_{RX} \downarrow$ | $\eta_{RY} \downarrow$ | $\eta_{RZ} \downarrow$ | $\iota \uparrow$    | $\eta_{RX} \downarrow$ | $\eta_{RY} \downarrow$ | $\eta_{RZ} \downarrow$ |
| Tram   | 0.248            | 0.363                  | <b>0.129</b>           | 0.489                  | 0.366            | 0.442                | 0.183                  | 0.623                  | 0.507                  | <b>0.667</b>        | <b>0.030</b>           | 0.191                  | <b>0.083</b>           |
| Car    | 0.368            | 0.516                  | 0.496                  | 0.538                  | 0.785            | 0.814                | 0.402                  | 0.308                  | 0.332                  | <b>0.842</b>        | <b>0.014</b>           | <b>0.159</b>           | <b>0.110</b>           |
| Truck  | 0.219            | 0.341                  | 0.243                  | 0.229                  | 0.216            | 0.433                | 0.086                  | 0.121                  | 0.159                  | <b>0.746</b>        | <b>0.009</b>           | <b>0.082</b>           | <b>0.032</b>           |
| Van    | 0.136            | 0.374                  | 0.139                  | 0.436                  | 0.538            | 0.528                | 0.381                  | <b>0.036</b>           | <b>0.070</b>           | <b>0.784</b>        | <b>0.007</b>           | 0.155                  | 0.142                  |
| Pedes. | 0.317            | 0.238                  | 0.422                  | 0.485                  | 0.429            | 0.619                | 0.175                  | 0.617                  | 0.598                  | <b>0.828</b>        | <b>0.043</b>           | <b>0.376</b>           | <b>0.407</b>           |
| Mean   | 0.276            | 0.366                  | 0.426                  | 0.435                  | 0.469            | 0.567                | 0.245                  | 0.341                  | 0.333                  | <b>0.773</b>        | <b>0.021</b>           | <b>0.193</b>           | <b>0.155</b>           |

## 4.2. SMOPE-Net Implementation Details

Our SMOPE-Net is implemented using the PyTorch library [12]. We use AdamW [18] optimizer to train the network on NVIDIA GeForce GTX Titan GPU for 200 epochs, using a learning rate of  $2e-4$ . On the KITTI-6DoF dataset, the hyper-parameters  $\alpha_1 - \alpha_5$  and  $\gamma_1, \gamma_2$  are respectively set to 6.0, 100.0, 100.0, 1.0, 10.0, 0.5, 3.0. For the LineMod dataset [4], the corresponding values are 90.0, 50.0, 50.0, 0.5, 5.0, 0.5, 10.0. Based on the TOPL method, the LabelImg3D tool is implemented using the PyQT Python binding and the VTK visualisation toolkit, which are open source softwares.

## 4.3. SMOPE-Net Evaluation

We evaluate the proposed SMOPE-Net on KITTI-6DoF and LineMod [4] datasets.

### 4.3.1 SMOPE-Net on KITTI-6DoF

Detailed in the supplementary material, a unique aspect of the KITTI-6DoF dataset is the large object to camera distances, a practical scenario in traffic scenes. Unfortunately, the traditional ADD metric [38] is adversely influenced by large object size and camera distance, proving to be unsuitable for KITTI-6DoF evaluation. Hence, an appropriate

metric for KITTI-6DoF evaluation is required, that accounts for the large object sizes and distances to camera. For this purpose, we propose the Gaussian distance as the metric to evaluate the translation of the pose as

$$\iota = e^{-\sqrt{(x_p - x_g)^2 + (y_p - y_g)^2 + (z_p - z_g)^2}}, \quad (9)$$

where  $(x_p, y_p, z_p)$  is the predicted object's center and  $(x_g, y_g, z_g)$  is its ground truth. For the rotation, we measure  $\eta_R$  based on the Euler angles as

$$\eta_{RX} = |r_{xg} - r_{xp}|, \quad \eta_{RY} = |r_{yg} - r_{yp}|, \quad \eta_{RZ} = |r_{zg} - r_{zp}|, \quad (10)$$

where  $r_g, r_p$  are the predicted and ground truth angles.

Table 5 summarizes the performance of our network on KITTI-6DoF. For comparison, we also provide results of BB8 [28], PVNet [26], and EfficientPose [5] for the same dataset. The best values are bold-faced. Our method provides a clear advantage in both rotation and translation accuracy compared to the existing related methods. Note that, PVNet only estimates the center and the 8 points of 3D bounding boxes in image space, from which only translation can be derived.

In Fig. 6, representative visual results of SMOPE-Net are shown for KITTI-6DoF. We also provide visual comparison of results achieved by our technique to existing methods

Table 6. Comparison on LineMod dataset using ADD scores [38].

| Method   | YOLO6D<br>[36] | Pix2Pose<br>[27] | PVNet<br>[26] | DPOD+<br>[40] | CDPN<br>[21] | Hybrid-Pose<br>[33] | EfficientPose<br>[5] | Ours          |
|----------|----------------|------------------|---------------|---------------|--------------|---------------------|----------------------|---------------|
| ape      | 21.62          | 58.10            | 43.62         | 87.73         | 64.38        | 63.10               | 89.43                | <b>96.24</b>  |
| bench    | 81.80          | 91.00            | 99.90         | 98.45         | 97.77        | 99.90               | 99.71                | <b>100.00</b> |
| can      | 68.80          | 84.40            | 95.47         | 99.71         | 95.87        | 98.50               | 99.70                | <b>100.00</b> |
| cat      | 41.82          | 65.00            | 79.34         | 94.71         | 83.83        | 89.40               | 96.21                | <b>100.00</b> |
| driller  | 63.51          | 76.30            | 96.43         | 98.80         | 96.23        | 98.50               | 99.50                | <b>100.00</b> |
| duck     | 27.23          | 43.80            | 52.58         | 86.29         | 66.76        | 65.00               | <b>89.20</b>         | 80.87         |
| eggbox   | 69.58          | 96.80            | 99.15         | 99.91         | 99.72        | <b>100.00</b>       | <b>100.00</b>        | <b>100.00</b> |
| glue     | 80.02          | 79.40            | 95.66         | 96.82         | 99.61        | 98.80               | <b>100.00</b>        | <b>100.00</b> |
| holepun. | 42.63          | 74.80            | 81.92         | 86.87         | 85.82        | 89.70               | 95.72                | <b>100.00</b> |
| Average  | 55.22          | 74.40            | 82.67         | 94.37         | 87.78        | 89.21               | 96.61                | <b>97.45</b>  |

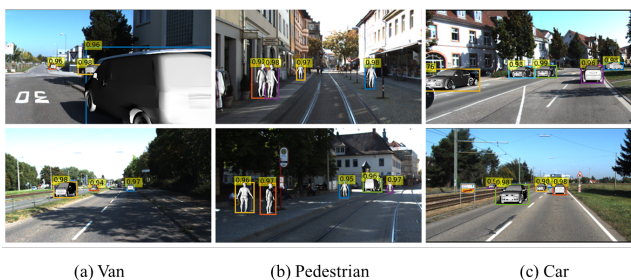


Figure 6. Qualitative results of SMOPE-Net on KITTI-6DoF for representative object categories. Best viewed in zoom in.

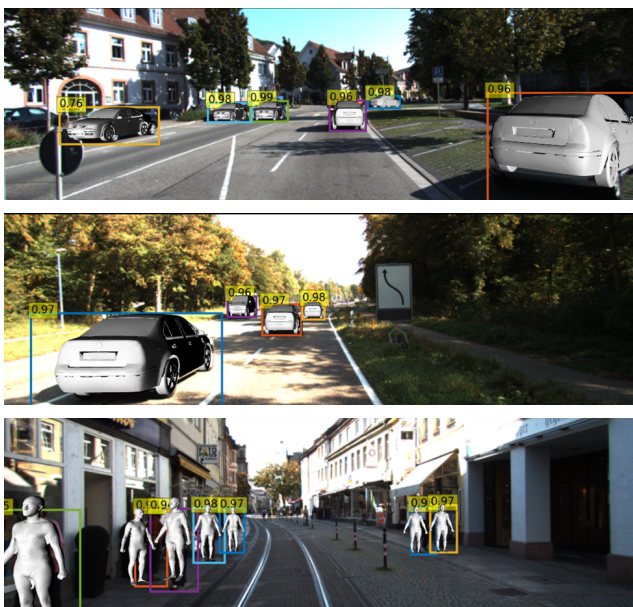


Figure 7. Results of SMOPE-Net on KITTI-6DoF dataset for multiple object detection and pose estimation tasks.

in Fig. 5. It can be seen that the detection and pose estimation results of our method are visibly better than other methods. In our experiments, we observed this to be true in general. It is also noteworthy that as compared to BB8 [28]

and PVNet [26], our method performs *multiple* object detection and pose estimation in a single shot, as shown in Fig. 7. Moreover, our method does not require a mask of the image object per frame for training or inference, which makes it more pragmatic.

#### 4.3.2 SMOPE-Net on LineMod

We also evaluate our approach on the LineMod dataset with the commonly used metric “ADD” for asymmetric objects [38]. This metric calculates the average point distances between the point set of the 3D models transformed by the estimated and ground truth rotations and translations. The estimated pose is considered correct if the ADD value is smaller than 10% of the object’s diameter. In Table 6, we compare our results with the current state-of-the-art methods. Our method outperforms all while only using the RGB image as input and without requiring any additional refinement. We emphasize that the performance gain of our technique comes in addition to the advantageous ability of simultaneously performing MOD & PE tasks in a single network, SMOPE-Net.

#### 4.4. Ablation Study

We conduct ablation studies to evaluate the contribution of different sub-networks and loss functions on model performance, using the KITTI-6DoF dataset. Tab. 7 and Tab. 8 summarize the results of our experiments. In Tab. 7,  $\ominus$ 3D-Model indicates removal of the 3D Encoder-Decoder, and  $\ominus$ 1st-fusion indicates the removal of the fusion branch between 3D Encoder and 3D Attention. It is apparent that both components considerably improve the performance in a complementary manner. To show the contributions of different sub-losses, we remove the farthest point sampling loss ( $\mathcal{L}_{fps}$ ), the point scales and centers loss ( $\mathcal{L}_{psc}$ ), the chamfer distance loss ( $\mathcal{L}_{cd}$ ) and the mesh edge loss ( $\mathcal{L}_{me}$ ) respectively, and report results in Tab. 8.



Table 7. Ablation analysis for the network structure.

| Network                    | $\iota \uparrow$ | $\eta_{RX} \downarrow$ | $\eta_{RY} \downarrow$ | $\eta_{RZ} \downarrow$ |
|----------------------------|------------------|------------------------|------------------------|------------------------|
| SMOPE $\ominus$ 3D-Model   | 0.534            | 0.026                  | 0.326                  | 0.582                  |
| SMOPE $\ominus$ 1st-fusion | 0.576            | 0.028                  | 0.257                  | 0.393                  |
| SMOPE                      | <b>0.773</b>     | <b>0.021</b>           | <b>0.193</b>           | <b>0.155</b>           |

Table 8. Ablation analysis for the loss. The  $\ominus$  denotes the network without the specified sub-loss.

| Loss  | $\iota \uparrow$ | $\eta_{RX} \downarrow$ | $\eta_{RY} \downarrow$ | $\eta_{RZ} \downarrow$ |
|---|------------------|------------------------|------------------------|------------------------|
| $\mathcal{L} \ominus \mathcal{L}_{fps}$                         | 0.505            | 0.046                  | 0.438                  | 0.678                  |
| $\mathcal{L} \ominus \mathcal{L}_{psc}$                         | 0.399            | 0.073                  | 0.435                  | 0.605                  |
| $\mathcal{L} \ominus \mathcal{L}_{cd} \ominus \mathcal{L}_{me}$ | 0.413            | 0.106                  | 0.585                  | 0.606                  |
| $\mathcal{L}$   | <b>0.773</b>     | <b>0.021</b>           | <b>0.193</b>           | <b>0.155</b>           |

## 5. CONCLUSION

In this paper, we made multiple important contributions towards the 6DoF estimation task. We introduced the unique concept of simultaneously dealing with multiple object detection and pose estimation with an end-to-end trainable neural model - SMOPE-Net. We thoroughly evaluated SMOPE-Net on two large datasets, achieving a significant performance gain over the existing methods. We also proposed KITTI-6DoF dataset, which provides 6DoF annotations for over 7K frames of the KITTI dataset. This dataset is created by an efficient tool, LabelImg3D, also proposed in this work. At the core of this tool is a twin space object labeling technique, which we developed to efficiently label 2D frames using 3D models of the objects therein. We establish the accuracy of our method analytically and empirically. We will publicly release our tool, dataset and the models resulting from this work after acceptance.

## References

- [1] Morteza Alizadeh, Michael Hamilton, Parker Jones, Junfeng Ma, and Raed Jaradat. Vehicle operating state anomaly detection and results virtual reality interpretation. *Expert Systems with Applications*, 177:114928, 2021. 1
- [2] Qiang Bai, Shaobo Li, Jing Yang, Qisong Song, Zhiang Li, and Xingxing Zhang. Object detection recognition and robot grasping based on machine learning: A survey. *IEEE Access*, 8:181855–181879, 2020. 1
- [3] Jens Behley, Andres Milioto, and Cyrill Stachniss. A benchmark for lidar-based panoptic segmentation based on kitti. In *2021 IEEE International Conference on Robotics and Automation (ICRA)*, pages 13596–13603. IEEE, 2021. 5, 6
- [4] Eric Brachmann, Alexander Krull, Frank Michel, Stefan Gumhold, Jamie Shotton, and Carsten Rother. Learning 6d object pose estimation using 3d object coordinates. In *European conference on computer vision*, pages 536–551. Springer, 2014. 2, 3, 6, 7
- [5] et al. Buks. Efficientpose: An efficient, accurate and scalable end-to-end 6d multi object pose estimation approach. *arXiv preprint arXiv:2011.04307*, 2020. 1, 2, 3, 7, 8
- [6] Yingfeng Cai, Tianyu Luan, Hongbo Gao, Hai Wang, Long Chen, Yicheng Li, Miguel Angel Sotelo, and Zhixiong Li. Yolov4-5d: An effective and efficient object detector for autonomous driving. *IEEE Transactions on Instrumentation and Measurement*, 70:1–13, 2021. 1
- [7] Nicolas Carion, Francisco Massa, Gabriel Synnaeve, Nicolas Usunier, Alexander Kirillov, and Sergey Zagoruyko. End-to-end object detection with transformers. In *European conference on computer vision*, pages 213–229. Springer, 2020. 3, 4
- [8] Long Chen, Han Yang, Chenrui Wu, and Shiqing Wu. Mp6d: An rgb-d dataset for metal parts 6d pose estimation. *IEEE Robotics and Automation Letters*, 2022. 3
- [9] Yujing Chen, Dong Wang, and Gongbing Bi. An image edge recognition approach based on multi-operator dynamic weight detection in virtual reality scenario. *Cluster Computing*, 22(4):8069–8077, 2019. 1
- [10] Francisco Chinesta, Elias Cueto, Emmanuelle Abisset-Chavanne, Jean Louis Duval, and Fouad El Khaldi. Virtual, digital and hybrid twins: a new paradigm in data-based engineering and engineered data. *Archives of computational methods in engineering*, 27(1):105–134, 2020. 1
- [11] Guoguang Du, Kai Wang, Shiguo Lian, and Kaiyong Zhao. Vision-based robotic grasping from object localization, object pose estimation to grasp estimation for parallel grippers: a review. *Artificial Intelligence Review*, 54(3):1677–1734, 2021. 1
- [12] Matthias Fey and Jan Eric Lenssen. Fast graph representation learning with pytorch geometric. *arXiv preprint arXiv:1903.02428*, 2019. 7
- [13] Andreas Geiger, Philip Lenz, Christoph Stiller, and Raquel Urtasun. Vision meets robotics: The kitti dataset. *The International Journal of Robotics Research*, 32(11):1231–1237, 2013. 2, 6
- [14] Ross Girshick. Fast r-cnn. In *Proceedings of the IEEE international conference on computer vision*, pages 1440–1448, 2015. 3
- [15] Kaiming He, Georgia Gkioxari, Piotr Dollár, and Ross Girshick. Mask r-cnn. In *Proceedings of the IEEE international conference on computer vision*, pages 2961–2969, 2017. 3
- [16] Stefan Hinterstoisser, Vincent Lepetit, Slobodan Ilic, Stefan Holzer, Gary Bradski, Kurt Konolige, and Nassir Navab. Model based training, detection and pose estimation of texture-less 3d objects in heavily cluttered scenes. In *Asian conference on computer vision*, pages 548–562. Springer, 2012. 2, 3, 6
- [17] Tomáš Hodan, Pavel Haluza, Štěpán Obdržálek, Jiri Matas, Manolis Lourakis, and Xenophon Zabulis. T-less: An rgb-d dataset for 6d pose estimation of texture-less objects. In *2017 IEEE Winter Conference on Applications of Computer Vision (WACV)*, pages 880–888. IEEE, 2017. 3
- [18] M Kalfaoglu, Sinan Kalkan, and A Aydin Alatan. Late temporal modeling in 3d cnn architectures with bert for action recognition. In *European Conference on Computer Vision*, pages 731–747. Springer, 2020. 7

- [19] Roman Kaskman, Sergey Zakharov, Ivan Shugurov, and Slobodan Ilic. Homebreweddb: Rgb-d dataset for 6d pose estimation of 3d objects. In *Proceedings of the IEEE/CVF International Conference on Computer Vision Workshops*, pages 0–0, 2019. 3
- [20] Wadim Kehl, Fabian Manhardt, Federico Tombari, Slobodan Ilic, and Nassir Navab. Ssd-6d: Making rgb-based 3d detection and 6d pose estimation great again. In *Proceedings of the IEEE international conference on computer vision*, pages 1521–1529, 2017. 2
- [21] et al. Li. Cdpn: Coordinates-based disentangled pose network for real-time rgb-based 6-dof object pose estimation. In *Proceedings of the IEEE/CVF International Conference on Computer Vision*, pages 7678–7687, 2019. 8
- [22] Guofa Li, Yifan Yang, Xingda Qu, Dongpu Cao, and Keqiang Li. A deep learning based image enhancement approach for autonomous driving at night. *Knowledge-Based Systems*, 213:106617, 2021. 1
- [23] Shaoshan Liu, Liangkai Liu, Jie Tang, Bo Yu, Yifan Wang, and Weisong Shi. Edge computing for autonomous driving: Opportunities and challenges. *Proceedings of the IEEE*, 107(8):1697–1716, 2019. 1
- [24] Wei Liu, Dragomir Anguelov, Dumitru Erhan, Christian Szegedy, Scott Reed, Cheng-Yang Fu, and Alexander C Berg. Ssd: Single shot multibox detector. In *European conference on computer vision*, pages 21–37. Springer, 2016. 2, 3
- [25] Kuan-Yu Lung, Chi-Rung Chang, Shao-En Weng, Hao-Siang Lin, Hong-Han Shuai, and Wen-Huang Cheng. Rosnet: Robust one-stage network for ct lesion detection. *Pattern Recognition Letters*, 144:82–88, 2021. 3
- [26] et al. P. Pvnet: Pixel-wise voting network for 6dof pose estimation. In *Proceedings of the IEEE/CVF Conference on Computer Vision and Pattern Recognition*, pages 4561–4570, 2019. 1, 3, 7, 8
- [27] et al. Park. Pix2pose: Pixel-wise coordinate regression of objects for 6d pose estimation. In *Proceedings of the IEEE/CVF International Conference on Computer Vision*, pages 7668–7677, 2019. 1, 3, 8
- [28] Mahdi Rad and Vincent Lepetit. Bb8: A scalable, accurate, robust to partial occlusion method for predicting the 3d poses of challenging objects without using depth. In *Proceedings of the IEEE international conference on computer vision*, pages 3828–3836, 2017. 7, 8
- [29] Shaoqing Ren, Kaiming He, Ross Girshick, and Jian Sun. Faster r-cnn: Towards real-time object detection with region proposal networks. *Advances in neural information processing systems*, 28, 2015. 3
- [30] Colin Rennie, Rahul Shome, Kostas E Bekris, and Alberto F De Souza. A dataset for improved rgb-d based object detection and pose estimation for warehouse pick-and-place. *IEEE Robotics and Automation Letters*, 1(2):1179–1185, 2016. 3
- [31] William J Schroeder, Lisa Sobierajski Avila, and William Hoffman. Visualizing with vtk: a tutorial. *IEEE Computer graphics and applications*, 20(5):20–27, 2000. 5
- [32] Liuguo Shao, Xiao Yu, and Chao Feng. Evaluating the eco-efficiency of china’s industrial sectors: A two-stage network data envelopment analysis. *Journal of environmental management*, 247:551–560, 2019. 3
- [33] et al. Song. Hybridpose: 6d object pose estimation under hybrid representations. In *Proceedings of the IEEE/CVF conference on computer vision and pattern recognition*, pages 431–440, 2020. 1, 3, 8
- [34] Martin Sundermeyer, Zoltan-Csaba Marton, Maximilian Durner, Manuel Brucker, and Rudolph Triebel. Implicit 3d orientation learning for 6d object detection from rgb images. In *Proceedings of the european conference on computer vision (ECCV)*, pages 699–715, 2018. 2
- [35] Mingxing Tan, Ruoming Pang, and Quoc V Le. Efficientdet: Scalable and efficient object detection. In *Proceedings of the IEEE/CVF conference on computer vision and pattern recognition*, pages 10781–10790, 2020. 1, 5
- [36] et al. Tekin. Real-time seamless single shot 6d object pose prediction. In *Proceedings of the IEEE Conference on Computer Vision and Pattern Recognition (CVPR)*, June 2018. 8
- [37] Dong Wang, Yuan Zhang, Kexin Zhang, and Liwei Wang. Focalmix: Semi-supervised learning for 3d medical image detection. In *Proceedings of the IEEE/CVF Conference on Computer Vision and Pattern Recognition*, pages 3951–3960, 2020. 1
- [38] Yongming Wen, Yiquan Fang, Junhao Cai, Kimwa Tung, and Hui Cheng. Gccn: Geometric constraint co-attention network for 6d object pose estimation. *Proceedings of the 29th ACM International Conference on Multimedia*, 2021. 7, 8
- [39] Yu Xiang, Tanner Schmidt, Venkatraman Narayanan, and Dieter Fox. Posecnn: A convolutional neural network for 6d object pose estimation in cluttered scenes. *arXiv preprint arXiv:1711.00199*, 2017. 2, 3, 6
- [40] et al. Zakh. Dpod: 6d pose object detector and refiner. In *Proceedings of the IEEE/CVF international conference on computer vision*, pages 1941–1950, 2019. 3, 8
- [41] Shifeng Zhang, Longyin Wen, Xiao Bian, Zhen Lei, and Stan Z Li. Single-shot refinement neural network for object detection. In *Proceedings of the IEEE conference on computer vision and pattern recognition*, pages 4203–4212, 2018. 3
- [42] Zhilu Zhang and Mert Sabuncu. Generalized cross entropy loss for training deep neural networks with noisy labels. *Advances in neural information processing systems*, 31, 2018. 5
- [43] Zhong-Qiu Zhao, Peng Zheng, Shou-tao Xu, and Xindong Wu. Object detection with deep learning: A review. *IEEE transactions on neural networks and learning systems*, 30(11):3212–3232, 2019. 1
- [44] Xingkui Zhu, Shuchang Lyu, Xu Wang, and Qi Zhao. Tph-yolov5: Improved yolov5 based on transformer prediction head for object detection on drone-captured scenarios. In *Proceedings of the IEEE/CVF International Conference on Computer Vision*, pages 2778–2788, 2021. 3
- [45] Xizhou Zhu, Weijie Su, Lewei Lu, Bin Li, Xiaogang Wang, and Jifeng Dai. Deformable detr: Deformable transformers for end-to-end object detection. *arXiv preprint arXiv:2010.04159*, 2020. 4

# Simultaneous Multiple Object Detection and Pose Estimation using 3D Model Infusion with Monocular Vision (Supplementary Material)

Congliang Li \*  
Chang'an University  
Xi'an, Shannxi, China  
congliangli@chd.edu.com

Shijie Sun \*  
Chang'an University  
Xi'an, Shannxi, China  
shijieSun@chd.edu.cn

Xiangyu Song †  
Swinburne University of Technology  
Melbourne, Australia  
xsong@swin.edu.au

Huansheng Song  
Chang'an University  
Xi'an, Shannxi, China  
hshsong@chd.edu.cn

Naveed Akhtar  
University of Western Australia  
Perth, Western Australia, Australia  
naveed.akhtar@uwa.edu.au

Ajmal Saeed Mian  
University of Western Australia  
Perth, Western Australia, Australia  
ajmal.mian@uwa.edu.au

## 1. Public Source Code & Dataset

Along with the submitted manuscript, we publish the KITTI-6DoF dataset, the source code of the SMOPE-Net, and the source code of the LabelImg3D for labeling the 6DoF pose of objects with the 3D models and a single image. For the sake of reviewing, the published repositories are anonymous and listed as follows (Click on the highlighted text to open the URL).

- **SMOPE-Net** is the source code of SMOPE-Net. It also contains the training and testing script for both LineMod [2] and KITTI-6DoF dataset, and instructions for reproducing the result of our methods.
- **LabelImg3D** is the source code of LabelImg3D. It also contains the instructions and usage of LabelImg3D.
- **KITTI-6DoF** provides the link to the dataset along with the related description.

## 2. Mathematical Proof Of the TOPL Method

The TOPL method estimates the pose of an object by creating a virtual twin space in which a virtual camera with the same focal length as the real camera is placed. Thus, it is imperative to prove the correctness of the method. That is, we need to ascertain that once the 3D model in the image generated by the Secondary Projection matches the real

object, the pose of the 3D model in the virtual camera coordinate is consistent with the real object's pose. This can be confirmed by proving that the relationship between the projection image and the pose of the object is bijective.

Denote a point in the object coordinate, world coordinate, camera coordinate, and image coordinate as  $p_o = (x_o \ y_o \ z_o \ 1)$ ,  $p_w = (x_w \ y_w \ z_w \ 1)$ ,  $p_c = (x_c \ y_c \ z_c \ 1)$  and  $p_i = (u \ v \ 1)$ , respectively. Denote a general transformation from coordinate  $A$  to coordinate  $B$  as  $P_{A \rightarrow B}$  and the rotation and translations as  $R_{A \rightarrow B}$  and  $T_{A \rightarrow B}$ , respectively. In the text below,  $O, W, C, I$  represent the object, world, camera, and image coordinates, respectively.

The transformation from the  $p_o$  to  $p_i$  can be written as

$$p_i = P_{O \rightarrow I} p_o. \quad (1)$$

where we can expand  $P_{O \rightarrow I}$  as

$$P_{O \rightarrow I} = P_{C \rightarrow I} \begin{bmatrix} R_{O \rightarrow C} & T_{O \rightarrow C} \\ \mathbf{0} & 1 \end{bmatrix} = \begin{bmatrix} R_{O \rightarrow W} R_{W \rightarrow C} & T_{O \rightarrow C} \\ \mathbf{0} & 1 \end{bmatrix}. \quad (2)$$

Here, the  $P_{C \rightarrow I}$  can be expressed as

$$P_{C \rightarrow I} = \frac{1}{\alpha} \begin{bmatrix} f & 0 & c_x \\ 0 & f & c_y \\ 0 & 0 & 1 \end{bmatrix} \begin{bmatrix} 1 & 0 & 0 & 0 \\ 0 & 1 & 0 & 0 \\ 0 & 0 & 1 & 0 \end{bmatrix}. \quad (3)$$

where  $c_x, c_y$  are the image center coordinates and  $\alpha$  is the

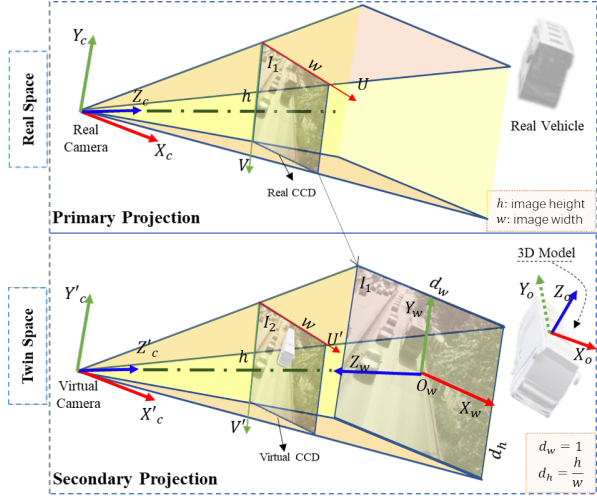


Figure 1. TOPL method. In Primary Projection, real camera captures the real objects in a Real Space. To simulate the Primary Projection, a virtual Twin Space is built, which contains 3D models with the same size as the real objects, a virtual camera with the same focal length as the real camera and the captured images of size  $d_w \times d_h$ . In Secondary Projection, a virtual camera captures the 3D models and the image in the Twin Space.  $X_c Y_c Z_c, UV$  are the camera coordinate and the image coordinates of the real scene.  $X'_c Y'_c Z'_c, U' V', X_w Y_w Z_w, X_o Y_o Z_o$  are the camera coordinates, the image coordinates, the world coordinates, and the model object coordinates in the Twin Space respectively.

scale factor. In Eq. (2), the  $T_{O \rightarrow C}$  is computed as

$$T_{O \rightarrow C} = \begin{bmatrix} -x_w & -y_w & -z_w - d \end{bmatrix}. \quad (4)$$

Similarly, the  $R_{O \rightarrow W}$  is as follows.

$$R_{O \rightarrow W} = \begin{bmatrix} 1 & 0 & 0 \\ 0 & \cos r_x & -\sin r_x \\ 0 & \sin r_x & \cos r_x \end{bmatrix} \begin{bmatrix} \cos r_y & 0 & \sin r_y \\ 0 & 1 & 0 \\ -\sin r_y & 0 & \cos r_y \end{bmatrix} \begin{bmatrix} \cos r_z & -\sin r_z & 0 \\ \sin r_z & \cos r_z & 0 \\ 0 & 0 & 1 \end{bmatrix} \quad (5)$$

Let us denote

$$q = \begin{bmatrix} \cos r_y \cos r_z \\ \sin r_x \sin r_y \sin r_z + \cos r_x \sin r_z \\ -\cos r_x \sin r_y \cos r_z + \sin r_x \sin r_z \end{bmatrix},$$

$$r = \begin{bmatrix} -\cos r_y \sin r_z \\ -\sin r_x \sin r_y \sin r_z + \cos r_x \cos r_z \\ \cos r_x \sin r_y \cos r_z + \sin r_x \sin r_z \end{bmatrix},$$

$$t = \begin{bmatrix} \sin r_y \\ -\sin r_x \cos r_y \\ \cos r_x \cos r_y \end{bmatrix},$$

the  $R_{O \rightarrow W}$  can be written as

$$R_{O \rightarrow W} = [q \quad r \quad t]. \quad (6)$$

The  $R_{W \rightarrow C}$  takes the form

$$R_{W \rightarrow C} = \begin{bmatrix} 1 & 0 & 0 \\ 0 & 1 & 0 \\ 0 & 0 & -1 \end{bmatrix} \begin{bmatrix} 0 & 1 & 0 \\ -1 & 0 & 0 \\ 0 & 0 & 1 \end{bmatrix} \begin{bmatrix} 0 & 1 & 0 \\ -1 & 0 & 0 \\ 0 & 0 & 1 \end{bmatrix} \quad (7)$$

Table 1. Comparison of 6DoF datasets. **O.N.**, **O.D.**, **C.O.D.** stand for the number of objects, the max diameter of objects, and the max distance from the camera to objects.

|           | Frames         | O.N.           | O.D.          | C.O.D.         |
|-----------|----------------|----------------|---------------|----------------|
| L-M [4]   | 15,800         | 15,800         | 0.283         | 1.169          |
| YCB-V [5] | <b>133,827</b> | <b>613,917</b> | 0.325         | 1.582          |
| Ours      | 7,481          | 27,665         | <b>16.605</b> | <b>150.818</b> |

Using Eq. 2–Eq.7 to compute the transformation in Eq. 1, we obtain an equation with 13 unknowns. Each pair of the 3D model point and its projection point on the 2D image can provide 3 equations. Therefore, the transformation is uniquely determined when at least 5 pairs of corresponding points exist. An asymmetric 3D object of fixed size has at least five pairs of known points. Hence, the relationship between its pose and projection remains bijective. Thus, for two cameras with the same focal length, if they capture asymmetric objects of the same size and the same pose, their projection image is bijective in relation to the pose. This fact is at the center of the effectiveness of our TOPL technique.

### 3. KITTI-6DoF Dataset

Utilizing the LabelImg3D, we label a subset of the KITTI dataset [3] with 3D models and create the “KITTI-6DoF” dataset, which provides additional annotations for 6DoF estimation, see Fig. 2. The KITTI-6DoF consists of 7,481 frames and provides annotations with five 3D models including Tram, Car, Van, Pedestrian, and Truck. To accommodate the differences in vehicle sizes in KITTI, we used the average size of each category for the 3D models. The models match closely to the objects in the frames. Fig. 3 visualizes the poses of LabelImg3D in Lidar coordinates of KITTI in red boxes, whereas green boxes are point cloud annotations labeled directly in Lidar coordinates. Consistency between the boxes is apparent.

We compare KITTI-6DoF with the existing dataset L-M [4] and YCB-V [5] in Table 1. The comparison is drawn along the number of images in the dataset, the total number of objects, the maximum diameter of the object outward sphere, and the maximum distance between the object and the camera. The diameter represents object size as the diameter of the object’s external sphere. An order of magnitude increase in the diameter and distance values is highly desirable for tasks related to large outdoor scenes.

We compare our proposed KITTI-6DoF dataset with the original KITTI 3D detection dataset [1] in Table 2. The comparison is drawn along the position, yaw, pitch, roll, 3D model and 3D size. Note that our dataset provides much more detailed information.



Figure 2. KITTI-6DoF dataset. Labeled by the proposed tool “LabelImg3D”, it consists of 7,481 frames. It uses five 3D models including Tram, Car, Van, Pedestrian, and Truck, which are well matched to the objects in the frames.

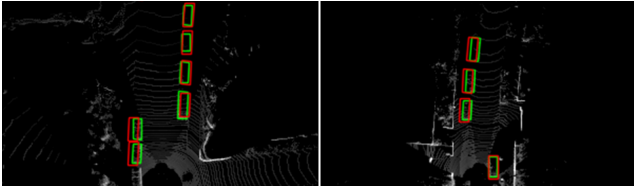


Figure 3. Consistency of KITTI-6DoF annotations with manual annotations. The green boxes are manual pose labels for Lidar data, the red boxes are KITTI-6DoF labels from 2D images.

Table 2. Comparison of our KITTI-6DoF dataset (with additional labels) to the original KITTI object 3D detection dataset. The original KITTI dataset does not provide two angles (Pitch and Roll) nor does it provide 3D models.

|           | Position | Yaw | Pitch | Roll | 3D Model | 3D Size |
|-----------|----------|-----|-------|------|----------|---------|
| KITTI [1] | ✓        | ✓   | ×     | ×    | ×        | ✓       |
| Ours      | ✓        | ✓   | ✓     | ✓    | ✓        | ✓       |

object pose estimation in cluttered scenes. *arXiv preprint arXiv:1711.00199*, 2017. 2

## References

- [1] Jens Behley, Andres Milioto, and Cyrill Stachniss. A benchmark for lidar-based panoptic segmentation based on kitti. In *2021 IEEE International Conference on Robotics and Automation (ICRA)*, pages 13596–13603. IEEE, 2021. 2, 3
- [2] Eric Brachmann, Alexander Krull, Frank Michel, Stefan Gumhold, Jamie Shotton, and Carsten Rother. Learning 6d object pose estimation using 3d object coordinates. In *European conference on computer vision*, pages 536–551. Springer, 2014. 1
- [3] Andreas Geiger, Philip Lenz, Christoph Stiller, and Raquel Urtasun. Vision meets robotics: The kitti dataset. *The International Journal of Robotics Research*, 32(11):1231–1237, 2013. 2
- [4] Stefan Hinterstoisser, Vincent Lepetit, Slobodan Ilic, Stefan Holzer, Gary Bradski, Kurt Konolige, and Nassir Navab. Model based training, detection and pose estimation of texture-less 3d objects in heavily cluttered scenes. In *Asian conference on computer vision*, pages 548–562. Springer, 2012. 2
- [5] Yu Xiang, Tanner Schmidt, Venkatraman Narayanan, and Dieter Fox. Posecnn: A convolutional neural network for 6d